# On the Use of Fly’s Eye Lenses with Leaky-Wave Feeds for Wideband Communications

Campo, Marta  Arias; Blanco, Darwin; Neto, Andrea; Llombart, Nuria; Bruni, Simona

**DOI**
10.1109/TAP.2019.2952474

**Publication date**
2020

**Document Version**
Final published version

**Published in**
IEEE Transactions on Antennas and Propagation

**Citation (APA)**
Campo, M. A., Blanco, D., Neto, A., Llombart, N., & Bruni, S. (2020). On the Use of Fly’s Eye Lenses with Leaky-Wave Feeds for Wideband Communications. *IEEE Transactions on Antennas and Propagation*, *68*(4), 2480-2493. Article 8961188. https://doi.org/10.1109/TAP.2019.2952474

# On the Use of Fly's Eye Lenses with Leaky-Wave Feeds for Wideband Communications

Marta Arias Campo, *Student Member, IEEE*, Darwin Blanco, Simona Bruni,
Andrea Neto, *Fellow, IEEE*, and Nuria Llombart, *Fellow, IEEE*

***Abstract*—In order to fulfill the exponential increase in the demand of high-speed wireless links, future XG wireless networks will be developed at higher carrier signal frequencies, reaching the hundreds of gigahertz. In this contribution, a leaky-wave-fed HDPE lens antenna working at *G*-band which can be useful for future XG communications is presented. The proposed lens design enables the generation of up to 40 beams, with gains higher than 30 dB. Analytical tools have been applied to optimize the lens aperture efficiency, validating the results via full-wave simulations. The reached aperture efficiency for the broadside beam is higher than 80% over a 44% relative bandwidth. The measurement results for a fabricated prototype show excellent agreement with the simulated performance.**

***Index Terms*—Leaky-wave antennas, lens antennas, multibeam antennas, wideband communications.**

## I. INTRODUCTION

NOWADAYS, wireless communication systems are experimenting a revolution, driven by new data-demanding applications. Future applications will need wireless links with capacities orders of magnitude larger than currently achieved in back-haul, front-haul, and access networks. Exploiting small RF bandwidths with advanced signal processing techniques has reached a saturation point, and therefore, other system alternatives need to be explored. One of the most reasonable approaches is to increase the RF carrier frequency, where larger bandwidths can be exploited to boost the maximum achieved throughput [1]. However, the wave-propagation spreading factor proportionally increases to the square of the frequency, and therefore, moving to higher frequency bands requires the use of high-gain antennas (>30 dB) to fulfill the link budget. Furthermore, transmitted power is limited at high frequencies, as upconverting chains are required, which exhibit low efficiencies. This fact magnifies the importance of achieving highly efficient front-ends and antennas.

In this article, we propose the use of wideband Fly's eye lens array architectures to generate multiple simultaneous fixed high-gain beams, in order to give coverage in future front-haul point-to-multipoint scenarios or access networks in dense small cells [Fig. 1(a)]. We consider multibeam systems with a single transceiver per beam or lens feeder. Possible application examples for the point-to-multipoint scenario are fixed wireless access connections, where a base station provides several buildings with internet broadband access, substituting fiber optics. Here, different beams in the base station point simultaneously at multiple static receivers situated in different buildings. An example for the second scenario, dense small cells, could be a football stadium, auditorium, or any crowded event. In this case, overlapping beams should simultaneously cover the whole field of view where the users are distributed [2].

The use of lens antennas allows to efficiently achieve larger gains >30 dBs, over larger bandwidths (>20%) in comparison with other more resonant antenna solutions, such as Fabry–Perot [3], metasurfaces [4], or transmitarrays [5]. Moreover, the lens-steering capability enables the generation of simultaneous multiple beams pointing in different directions with planar Fly's eye lens array panels, as displayed in Fig. 1(b). This facilitates the integration with high-frequency front-ends, which can be in this way mounted on a single printed circuit board (PCB) per panel. A high-gain beam with stable pointing angle over the whole bandwidth is achieved contrary to other frequency dispersive leaky-wave concepts (see [6], [7]). In order to arrive to a more compact antenna array, each lens can host several transceivers or beams. The number of beams per lens will be mainly limited by the size of the active circuitry in terms of wavelength. Maximizing the lens aperture efficiency allows to further reduce the lens array size.

Table I presents a summary of the performances for the most relevant designs of integrated lens antennas found in the literature. Materials with high dielectric permittivity, $\varepsilon_r$, such as silicon ($\varepsilon_r = 11.9$) or alumina ($\varepsilon_r = 9$) are chosen in many cases, presenting very low ohmic losses. The main disadvantage of these designs lays on the high reflection in the lens–air interface. There are several designs reported reaching high lens aperture efficiencies over a relative bandwidth of 15%–20% [8], [9]. Double-slot antennas [8] or waveguide

---

Manuscript received December 7, 2018; revised October 2, 2019; accepted October 6, 2019. Date of publication January 16, 2020; date of current version April 7, 2020. This work was supported by the European Union through the ERC Starting Grant LAA-THz-CC under Grant 639749. *(Corresponding author: Nuria Llombart.)*

Marta Arias Campo is with the THz Sensing Group, Delft University of Technology, 2628 CD Delft, The Netherlands, and also with IMST GmbH, 47475 Kamp-Lintfort, Germany (e-mail: m.ariascampo@tudelft.nl; arias@imst.de).

Darwin Blanco is with Ericsson AB, 417 56 Gothenburg, Sweden.

Simona Bruni is with IMST GmbH, 47475 Kamp-Lintfort, Germany.

Andrea Neto and Nuria Llombart are with the THz Sensing Group, Delft University of Technology, 2628 CD Delft, The Netherlands.

Color versions of one or more of the figures in this article are available online at http://ieeexplore.ieee.org.

Digital Object Identifier 10.1109/TAP.2019.2952474

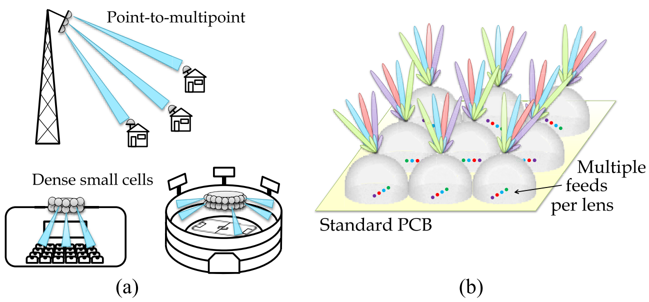

(a) (b)

Fig. 1. (a) Scenarios for fixed multibeam antenna architectures. (b) Planar lens array panel generating multiple fixed simultaneous beams.

TABLE I
SIMULATED PERFORMANCES OF INTEGRATED LENS ANTENNAS*

| Ref. | $f_0$ (GHz) | BW (%) | Dir. $f_0$ (dB) | Min $\eta_{ap}$ (dB) | Max $L_{diel}$ (dB) | Max. SLL (dB) |
|---|---|---|---|---|---|---|
| [8] | 246 | - | 29.9 | –1.1 | - | –16 |
| [9] | 60 | 16 | 19.9 | *–2.3* | - | –16 |
| [10] | 400 | 1:3 | 27 | *–2.6* | 0.2 | –8 |
| [11] | 50 | 1:5 | 19 | *–3.3* | 1.5 | –12.5 |
| [13] | 550 | 18 | 22.2 | *–1* | - | –15 |
| [14] | 77 | 10 | 24 | *–1.5* | 0.5 | –15 |
| [17] | 30 | 12.5 | 25.9 | *–1.9* | 0.5 | –14 |
| [18] | 73.5 | 7 | 37.3 | –2.9 | 1 | - |
| [19] | 290 | 30 | 31.5 | *–4* | - | –8 |
| This work | 180 | 44 | 34 | –1 | 0.5 | –15 |

(*) Values in italic have been extracted from the articles.

apertures [9] are usually used as lens feeders. Larger bandwidth designs are presented using double bow-tie antennas, in [10], and nonresonant leaky-wave antennas, in [11]. However, in both cases, the feed pattern which illuminates the lens surface does not allow for reaching high aperture efficiencies and higher sidelobe levels are reported. In [12] and [13], a resonant leaky-wave antenna (LWA) or Fabry–Perot antenna was proposed as a promising solution to act as a silicon lens feeder, due to its high directivity, symmetric pattern, compactness, low profile, and compatibility with silicon fabrication processes but presented narrow bandwidth. Designs using lenses in quartz ($\varepsilon_r = 3.8$) and MACOR™ material ($\varepsilon_r = 5.6$) have been reported in [14]–[16]. In [14], the beam quality is degraded due to the effects of multiple reflections. In [15], the feed pattern asymmetry results in lower lens aperture efficiency, presenting high reflection losses. In [16], the use of a shell with lower $\varepsilon_r$ improves the reflection efficiency and optimizes the lens-steering capabilities. Unfortunately, in both cases, the dielectric loss is very high, which leads to a considerable power loss (3.7–5.6 dB reported in [16]). Low $\varepsilon_r$ plastic materials ($\varepsilon_r \leq 2.5$) represent a good candidate to fabricate lens antenna arrays, due to the availability of moderate loss materials (HDPE, Rexolite, Topas), with light weight and enabling cost-effective manufacturing through processes such as injection molding or 3-D printing. Nevertheless, the efficient illumination of these lenses is more challenging. The larger lens eccentricity, $e$, needed for low $\varepsilon_r$ lenses implies that directive feeds are needed to avoid the lens critical angle. Most of the reported designs for lenses with $\varepsilon_r \leq 2.5$ present reflection issues which decrease the antenna efficiency and degrade the radiation pattern quality [17]–[19].

In this article, we extend the LWA feed architecture presented in [13] for low $\varepsilon_r$ lens materials. The goal is to achieve high gain with high aperture efficiency over a wide band, required for future wireless communication applications. A new methodology for the analysis and design of elliptical lenses illuminated by resonant LWAs is introduced, based on an analysis of the lens antenna in reception. This approach allows maximizing the aperture efficiency of the lens antenna by performing a field match between the geometrical optics frequency-independent field and the LWA field, avoiding more time-consuming parametric optimizations based on full wave (FW) or physical optics (PO). Design curves for the maximum aperture efficiency and bandwidth as a function of the lens $\varepsilon_r$ are in this way derived. The steering properties of elliptical lenses are also maximized here, for the first time, by introducing an optimal truncation in the lens geometry that trade-offs reflection and taper efficiencies. Most of the previous works in Table I considered nontruncated lenses. We present the maximum number of overlapping beams that may be achieved per planar lens array panel [Fig. 1(b)] as a function of different lens materials. Finally, we report an experimental validation of the performances for a low-density elliptical lens made with HDPE, leading to state-of-the-art performances. The simulation results show an aperture efficiency higher than 80%, matching better than $-10$ dB and ohmic losses lower than 0.5 dB over 44% relative bandwidth. The measurements are in very good agreement with the simulations.

This article is organized as follows. Section II describes the resonant LWA feeder concept. Section III describes the lens aperture efficiency optimization methodology. Section IV describes bandwidth properties of resonant LWAs in terms of aperture efficiency, as a function or the lens $\varepsilon_r$. Section V shows the scanning performances in truncated elliptical lenses with different $\varepsilon_r$. Sections VI and VII show the design and experimental results of a prototype fabricated in low $\varepsilon_r$ material.

## II. LENS FEEDER: RESONANT LEAKY-WAVE ANTENNA

The proposed feeder geometry is shown in Fig. 2. It consists of a resonant (Fabry–Perot) air cavity between a ground plane and a lens dielectric medium. The excitation of the air cavity is performed by means of a squared waveguide TE$_{01}$ mode illuminating a double-slot opening in the ground plane [Fig. 2(b) and (c)], similar approach to the one used in [20] and [21]. The double slot is used to further shape the pattern, as will be explained in following subsections, in order to maximize the aperture efficiency. It also plays an important role in the impedance matching to the waveguide. The squared waveguide size is fixed to $wg = 0.8\lambda_0$ at the central frequency [Fig. 2(b)], to avoid the excitation of higher order modes.

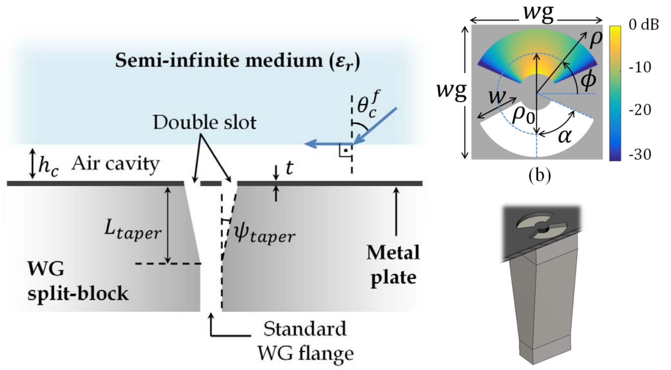

(a) (b) (c)

Fig. 2. (a) LWA geometry. A semi-infinite dielectric slab is located at a distance $h_c \sim \lambda_0/2$ to create a Fabry–Perot cavity illuminated by a tapered WG ($L_{taper} = 4.4\lambda_0$, $\psi_{taper} = 3°$). $\theta_c^f$ is the feed critical angle, after which the cavity presents total reflection. Blue arrows: incident and transmitted rays in the dielectric–air interface. (b) Main parameters of the double-slot iris and approximated magnetic current distribution from (8). (c) 3-D view of the tapered waveguide and double slot in the ground plane.

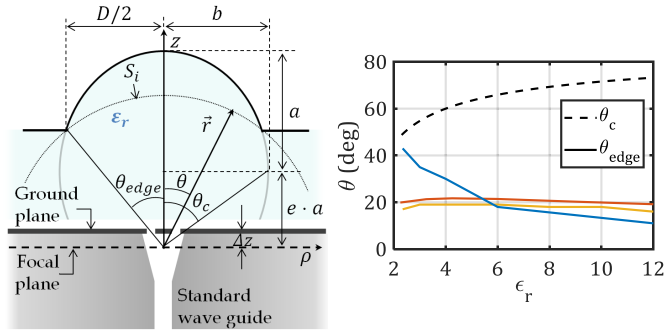

(a) (b)

Fig. 3. (a) Elliptical lens parameters are related as $a^2 = b^2 + (e \cdot a)^2$, and the focal distance is defined as $F = a + e \cdot a$. (b) Dashed line: lens critical angle, $\theta_c$, as shown in (a). Solid line: comparison of optimum lens edge truncation angles, $\theta_{edge}$, as defined in (a) where the blue line is $\theta_{edge}$ for maximum $\eta_{il}$ with the LWA as feeder, the red line is $\theta_{edge}$ for maximum steering angle applying the geometric criteria, and the yellow line is $\theta_{edge}$ for maximum steering angle with a cosine primary pattern extracted with PO.

The waveguide is then tapered to a standard flange as shown in Fig. 2(a) and (c). This tapering has minor impact on the radiation and impedance matching.

The physical phenomenon exploited in standard resonant LWAs or Fabry–Perot antennas is the excitation of a pair of nearly degenerated $TM_1/TE_1$ leaky-wave modes inside a resonant dielectric cavity [22], such as air, placed between a ground plane and a quarter wavelength dielectric substrate with higher $\varepsilon_r$ [Fig. 2(a)]. These modes propagate radially by means of multiple reflections along the cavity, leaking at the same time energy into the infinite dielectric medium. This effect increases the antenna effective area and thus, its directivity but at the cost of bandwidth [23]. In [12], it was shown that an enhancement in the *bandwidth* × *directivity* performance of a resonant LWA can be achieved by using a resonant air cavity below a semi-infinite dense medium (the lens), as displayed in Fig. 2(a). In this configuration, the LW modes present propagation phase constants $\beta_{LW} = k_0\sqrt{\varepsilon_r}\sin\theta_{LW} < k_0$, which implies that LW modes radiate always in elevation angles smaller than the feed critical angle [$\theta_c^f$ in Fig. 2(a)], and very low power is radiated at $\theta > \sin^{-1}(1/\sqrt{\varepsilon_r})$. Furthermore, in order to achieve a broadband design, it is convenient to choose a medium with low $\varepsilon_r$ to reduce the frequency dispersion of the $TM_1/TE_1$ leaky-wave modes [24].

## III. LENS APERTURE EFFICIENCY OPTIMIZATION

The proposed lens geometry is shown in Fig. 3(a). The lens is an elliptical surface characterized by an eccentricity $e = 1/\sqrt{\varepsilon_r}$ and truncated at an angle $\theta_{edge}$ defined from the bottom lens focus. The lens truncation helps to achieve high aperture efficiency when compared to more classical full hemispherical lens designs [8]. The LW ground plane is placed at a distance $\Delta z$ above the lens focal plane, since the phase center of LWAs is below the ground plane [25].

In order to evaluate the lens antenna aperture efficiency, $\eta_{ap}$, we propose an analysis in reception as detailed in the Appendix. The aperture efficiency can in this way be expressed as a field reaction between a frequency-independent analytical field and the field radiated by the feeder in an infinite dielectric medium. This approach in reception allows us to maximize the lens aperture efficiency by optimizing the lens feed geometry, its phase center position, $\Delta z$, and the lens $\theta_{edge}$, without performing the secondary pattern computation, which would be more time-consuming, as in more standard PO approaches [8].

The aperture efficiency for this focusing system can be evaluated dividing the power $P_L$ received by a matched load by the power captured by the lens aperture from the incident plane wave, $P_{in} = 1/(2\zeta_0)|E_0^{PW}|^2 A_{lens}$, being $A_{lens} = \pi D^2/4$ the projected area for a lens with diameter $D$ [Fig. 3(a)] and $E_0^{PW}$ the plane wave amplitude, as follows:

$$\eta_{ap} = \frac{P_L}{P_{in}} = \eta_{il}\eta_{ref}. \tag{1}$$

$\eta_{ap}$ accounts for the illumination efficiency and the reflection efficiency, and is equivalent to the ratio between the lens directivity and that of a uniform circular aperture. The efficiency $\eta_{il}$ represents the antenna efficiency assuming the use of a perfect matching layer in the whole frequency band. It accounts for taper and spillover efficiencies (power reaching the focal plane but not intercepted by the feed). $\eta_{ref}$ is the power reflected in the air–lens interface.

The power received by the load, $P_L$, as shown in the Appendix, can be expressed as a reaction integral between two terms: 1) the inward incident field inside the lens, $\vec{E}_{GO}^{S_i}$, caused by the broadside plane wave impinging on the lens, which is frequency independent, and 2) the field radiated in an infinite dielectric medium by the feed antenna considered in transmission, $\vec{E}_a^{GP}$, as

$$P_L = \frac{\left|\int_0^{2\pi}\int_0^{\theta_{edge}} \vec{E}_{GO}^{S_i}(\theta,\phi)\cdot\vec{E}_a^{GP}(\theta,\phi)e^{jk\Delta z cos\theta}R^2 sin\theta d\theta d\phi\right|^2}{4\zeta_d^2 P_{rad}} \tag{2}$$

where $P_{rad}$ is the total power radiated by the feed antenna in the infinite dielectric medium and $\zeta_d$ the wave impedance in

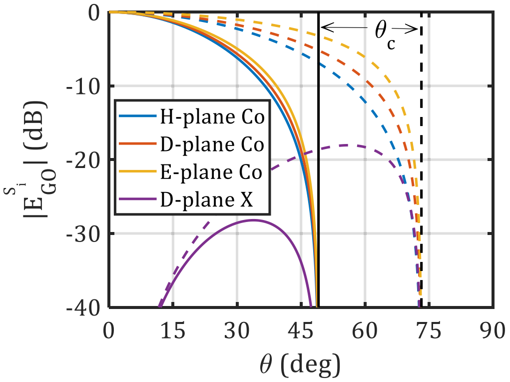

Fig. 4. Normalized $|E_{GO}^{S_i}|$ versus lens elevation angle $\theta$ over $S_i$, until lens critical angle. Solid line: $\varepsilon_r = 2.3$, dashed: $\varepsilon_r = 12$. The lens critical angles, $\theta_c$, are marked with black lines. Results shown with no matching layer.

the lens medium. The field reaction in (2) is evaluated over the truncated spherical surface $S_i$ [Fig. 3(a)] with radius $R$, centered at the lens focus and limited by the lens truncation angle, $\theta_{edge}$. The term $e^{jk\Delta z cos\theta}$ assumes that the lens is in the far-field of the feed antenna. $\vec{E}_{GO}^{S_i}$ can be approximated in $S_i$ as a superposition of local plane waves, whose amplitude can be analytically derived applying geometrical optics (GO) [26].

The aperture efficiency is maximized when the inward incident field, $\vec{E}_{GO}^{S_i}$, is a conjugate match (in terms of amplitude, phase, and polarization) with the field radiated by the feed antenna, $\vec{E}_a^{GP}$(2). Moreover, in order to achieve high reflection efficiency, $\eta_{ref}$, only the lens region above the lens critical angle, $\theta_c$, should be illuminated [top half of the ellipse, see Fig. 3(a)]. $\theta_c$ exclusively depends on the dielectric $\varepsilon_r$ and increases for higher values of $\varepsilon_r$ as $\theta_c = \tan^{-1}\sqrt{\varepsilon_r - 1}$ [Fig. 3(b)]. Thus, lenses with lower $\varepsilon_r$ need to be illuminated with more directive beams than denser lenses.

Fig. 4 shows the amplitude of the incident field, $\vec{E}_{GO}^{S_i}$, for nontruncated elliptical lenses in materials with $\varepsilon_r = 2.3$ and $\varepsilon_r = 12$, plotted until $\theta_c$. The phase of this field is constant over the chosen sphere $S_i$, where the integral in (2) is evaluated. The amplitude taper is mainly caused by the Fresnel transmission coefficients in the air–lens interface [26], which decay when approaching $\theta_c$. Here, lenses without matching layer have been considered. If a matching layer was introduced, the corresponding transmission coefficients would result in a more symmetric incident field, $\vec{E}_{GO}^{S_i}$, over $\phi$. A smaller contribution to this taper is originated by the power spreading factor in the refracted rays inside the lens. The lens eccentricity, $e$, increases for lower $\varepsilon_r$, resulting in a $\vec{E}_{GO}^{S_i}$ which approaches the cosine pattern. Instead, for high $\varepsilon_r$, where the lens approaches an spherical form, $\vec{E}_{GO}^{S_i}$ is closer to a squared pattern. In any case, both fields present a very low taper at the edges, differing very much to those corresponding to a parabolic reflector, where $\vec{E}_{GO}^{S_i}$ presents a secant shape [27].

## IV. BANDWIDTH PROPERTIES OF THE RESONANT LEAKY-WAVE LENS ANTENNA VERSUS $\varepsilon_r$

The analysis in reception described in Section III has been applied to quantify the LWA bandwidth in terms of pattern stability, or equivalently illumination efficiency, $\eta_{il}$, when acting as an integrated elliptical lens feeder. The LWA radiation patterns have been calculated with an asymptotic evaluation of the spectral Green's function (SGF) in stratified media [23], convoluted with a simplified current approximation for the double slot (Appendix). This approach allows us to optimize the feed-lens system aperture efficiency exclusively applying analytical tools. The first step to extract the bandwidth properties for different $\varepsilon_r$ is to calculate the optimum lens, LW cavity, and double-slot parameters which give the maximum $\eta_{il}$. Next, the relative bandwidth for these optimum cases is determined in terms of the lens $\eta_{il}$ over frequency.

When evaluating the resonant LWA as lens feeder, the main effect on the bandwidth is associated with the dispersion of the main leaky-wave modes [24]. However, the maximum $\eta_{il}$ highly depends on the spurious $TM_0$ contribution [28] (being $\theta_{TM_0}$ its radiation angle), which can radiate inside or outside the truncated lens rim, $\theta_{edge}$ [Fig. 3(a)]. The distance $\rho_0$ in the double slot [Fig. 2(b)] becomes a key parameter to optimize this maximum efficiency, as it is directly related to the position of a null in the Fourier transform (FT) of the double-slot equivalent currents, which can be used to further shape the pattern. The double slot, circular to achieve rotationally symmetric patterns, has been considered for this analysis with an angle $\alpha$ of 60° and width $w$ of $0.15\lambda_0$, being those realistic values to achieve a good matching to the waveguide.

In order to clarify the impact of the $TM_0$ radiation and double-slot distance in $\eta_{il}$, we analyze more deeply two extreme cases: $\varepsilon_r = 2.3$ and $\varepsilon_r = 12$. This $\varepsilon_r$-range is representative for most common lens materials found in the literature. Fig. 5 shows the far-field patterns of the resonant LWA, $\vec{E}_a$, for these two cases with maximum $\eta_{il}$, with an elementary excitation (left) and with the double-slot iris (right). For $\varepsilon_r = 12$, the feed critical angle [Fig. 2(a)] arrives at 16.7°, and so the radiation is confined in smaller angles. The lens should be, therefore, intuitively truncated at $\theta_{edge} \leq 17°$, in order to obtain high $\eta_{tap}$. $\vec{E}_{GO}^{S_i}$ presents an almost constant amplitude distribution at $S_i$ for $\theta < 17°$ [Figs. 4 and 5 (top)], and, therefore, a squared primary pattern is required in this case to reach a high $\eta_{tap}$. A cavity larger than the standard half wavelength, $h_c = 0.57\lambda_0$, contributes to the desired pattern form, as in this case the $TM_1/TE_1$ modes radiate toward larger angles [Fig. 5 (top left)]. The $TM_0$ mode radiation would reduce in this case the $\eta_{tap}$, and so the best compromise is to keep it out of the lens rim ($\theta_{edge} < \theta_{TM_0}$), as in [12] and [21]. In this way, the double slot should ideally fully cancel the effect of the $TM_0$, in order to reduce the spillover, by introducing a null in the FT of its equivalent currents at $\theta_{iris} \sim \theta_{TM_0}$, as shown in Fig. 5 (top right). The optimum double-slot $\rho_0$ is in this case around $0.64\lambda_0$. This is the best compromise between canceling completely the $TM_0$ (higher $\eta_{so}$) and keeping the pattern inside the lens rim as squared as possible (higher $\eta_{tap}$). The resulting optimum pattern for $\varepsilon_r = 12$ is shown in Fig. 5 (top right), where $\theta_{iris}$ can be clearly distinguished in the E-plane at $\theta = 15°$, lowering the $TM_0$ radiation peak in around 15 dB. The position of $\theta_{iris}$ has in case of high $\varepsilon_r$ materials similar dispersion characteristic as

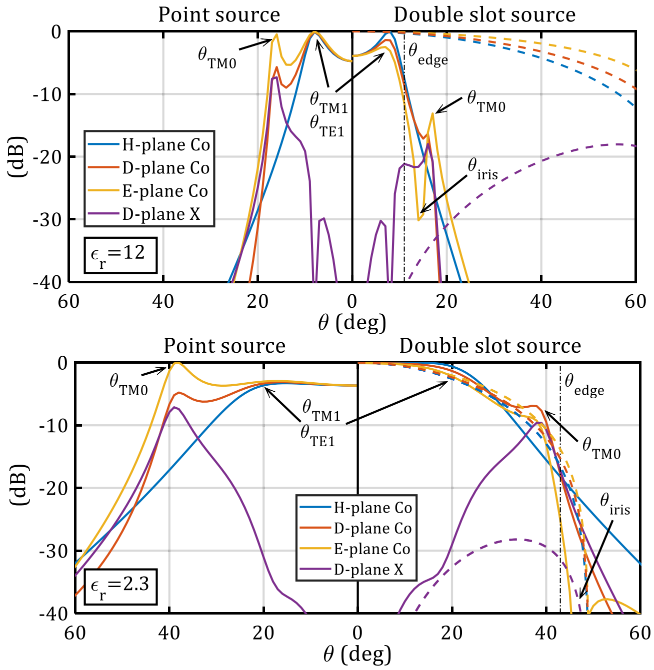

Fig. 5. LWA far-field patterns, $\vec{E}_a$, for $\varepsilon_r = 12$ (top) and $\varepsilon_r = 2.3$ (bottom). Left side: $x$-polarized elementary magnetic source. Right side: double-slot iris source. The shown patterns are symmetric with respect to $\theta$. For reference, $\vec{E}_{GO}^{S_i}$ at $S_i$ (dashed lines) is also plotted. All curves have been extracted using the geometric parameters (cavity, double slot, and lens) which maximize $\eta_{il}$. Those are $h_c = 0.56\lambda_0$, $\rho_0 = 0.5\lambda_0$, and $\theta_{edge} = 43°$ for $\varepsilon_r = 2.3$, and $h_c = 0.57\lambda_0$, $\rho_0 = 0.64\lambda_0$ and $\theta_{edge} = 11°$ for $\varepsilon_r = 12$.

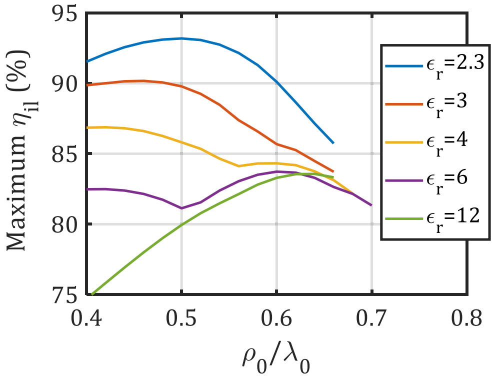

Fig. 6. Maximum $\eta_{il}$ versus double-slot distance $\rho_0$ normalized to $\lambda_0$. The rest of geometric parameters are optimized for every double-slot distance.

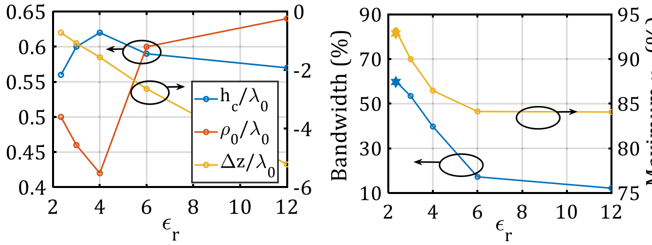

(a) (b)

Fig. 7. (a) Optimum cavity height, double-slot distance, and LWA phase center position for maximum $\eta_{il}$ versus lens $\varepsilon_r$. (b) LWA relative bandwidth for lens $\eta_{il} > 80\%$ as a function of $\varepsilon_r$, for a design with the maximum $\eta_{il}$, and maximum $\eta_{il}$ achieved versus $\varepsilon_r$. The stars represent the simulated values reached with the HDPE prototype.

the LWA TM$_1$/TE$_1$ and modes and, therefore, does not impact significantly in the relative bandwidth of the lens $\eta_{il}$.

For $\varepsilon_r = 2.3$, the feed critical angle arrives at 41°. The lens should be, therefore, truncated at $\theta_{edge} \leq 41°$, in order to obtain a high $\eta_{tap}$. For this angular range, $\vec{E}_{GO}^{S_i}$ presents an amplitude distribution at $S_i$ which approaches a cosine with approximately $-15$ dB taper [Figs. 4 and 5 (bottom)]. In this case, it is more convenient to choose $\theta_{edge} > \theta_{TM_0}$ and only taper down the TM$_0$ contribution by means of the double slot. The optimum $\rho_0$ is, therefore, $0.5\lambda_0$, for which the null in the FT of the double-slot equivalent currents $\theta_{iris} > \theta_{TM_0}$ [Fig. 5 (bottom right)]. The resulting LWA pattern [Fig. 5 (bottom right)] presents in this way a very similar taper to the incident field, reaching high $\eta_{tap}$. Here, $\theta_{iris}$ appears at around 45°, and the TM$_0$ radiation is tapered down to $-8$dB, being the high correlation between $\vec{E}_a$ and $\vec{E}_{GO}^{S_i}$ evident. For low $\varepsilon_r$, the position for $\theta_{iris}$, related to the optimum $\rho_0$, appears in the region beyond the feed critical angle, where very low power is radiated by the LWA. In this way, the narrow-band characteristic of the slot $\theta_{iris}$ has a small impact on the primary patterns. Their dispersion with frequency is consequently mostly related to the LW modes dispersion, which are very broadband for low $\varepsilon_r$. This fact provides these lenses with a very large $\eta_{il}$ bandwidth.

Fig. 6 shows the maximum reachable lens $\eta_{il}$ as a function of the double-slot distance, $\rho_0$ for several lens $\varepsilon_r$. We can observe that the overall maximum $\eta_{il}$ appears for $\varepsilon_r = 2.3$ thanks to the very good field correlation explained previously, achieved by keeping the TM$_0$ inside the lens rim and a double-slot distance of $\rho_0 \sim 0.5\lambda_0$. As we move to higher $\varepsilon_r$, a second relative maximum appears for $\rho_0 \sim 0.6\lambda_0$, becoming an absolute maximum for $\varepsilon_r = 12$, associated with the TM$_0$ radiating outside the lens rim. As the $\varepsilon_r$ increases from 2.3 to 4, the taper in $\vec{E}_{GO}^{S_i}$ decreases, demanding a lower value of amplitude taper to keep a high $\eta_{tap}$. The inflection point between these two design strategies appears at around $\varepsilon_r = 6$, where a good compromise between $\eta_{tap}$ and $\eta_{so}$ can be reached for both $\theta_{edge} < \theta_{TM_0}$ (optimum $\rho_0 = 0.6$) and $\theta_{edge} > \theta_{TM_0}$ (optimum $\rho_0 = 0.4$). If a wideband design is pursued, the design with $\theta_{edge} > \theta_{TM_0}$ and $\rho_0 = 0.4$ should be chosen, for which the frequency dispersion of $\theta_{iris}$ has a lower impact on the $\eta_{il}$ bandwidth.

Following this design approach, the LWA lens antenna has been optimized as a function of $\varepsilon_r$. The obtained parameters are summarized in Figs. 3(b) and 7(a). The relative frequency bandwidth for which $\eta_{il} > 80\%$ is achieved, as well as the maximum reached $\eta_{il}$ are reported in Fig. 7(b). Relative bandwidths higher than 40% can be achieved with $\varepsilon_r < 4$, whereas 15% bandwidth is reached with this criterion in case of using a lens with $\varepsilon_r \sim 12$.

## V. ELLIPTICAL LENS SCANNING PROPERTIES VERSUS $\varepsilon_r$

The lens-steering capability defines the maximum number of beams, overlapping at $-3$ dB, which can be generated with a single Fly's eye lens planar panel [Fig. 1(b)]. In [29],

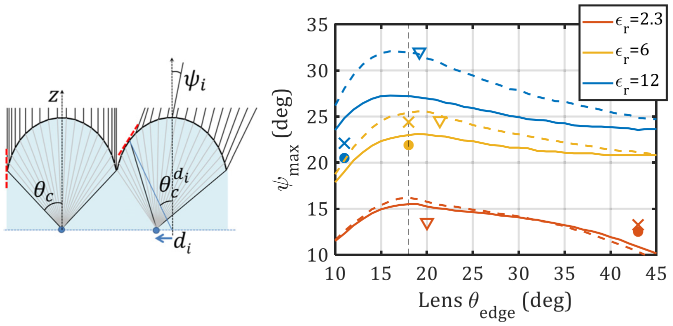

(a) (b)

Fig. 8. (a) Elliptical lens ray-tracing example for on- and off-focus feeds, where the lens critical angles are shown for both cases: $\theta_c$ and $\theta_c^{d_i}$, respectively. (b) Maximum steering angle $\psi_{max}$ achieved in free space versus lens $\theta_{edge}$. Triangles: geometric approximation. Solid line: PO analysis with cosine illumination for H-plane steering; dashed line: the same for E-plane. Circles: PO analysis with LW feed optimized for broadside for H-plane steering; crosses: the same for E-plane.

the steering properties of extended hemispherical lenses were studied for double-slot feeders. Here, instead, we investigate the steering capabilities of truncated elliptical lenses as function of the lens truncation angle, $\theta_{edge}$ [Fig. 3(a)], using ideal feeders adapted to each $\theta_{edge}$. The scope is to derive the optimum $\theta_{edge}$ that maximizes the steering angle (accepting 3 dB scan loss) and aperture efficiencies by making a tradeoff between the different loss mechanisms involved (taper, reflection, and spillover). The considered lens materials are the same as in Section IV. Finally, the steering capabilities for lenses with different $\varepsilon_r$ fed by the LWA are evaluated, completing the performance analysis for such feeders.

Displacing the feed a distance $d_i$ along the lens focal plane generates a beam-steering angle $\psi_i$ in the lens far-field [Fig. 8(a)]. $\psi_i$ can be geometrically approximated by tracing the central ray as $\psi_i = \sin^{-1}(\sqrt{\varepsilon_r}(d_i/F))$, being $F$ the lens focal distance [Fig. 3(a)]. It is clear that lower $\varepsilon_r$ materials need higher feed displacements to achieve a certain steering angle. In order to avoid significant spillover loss, the maximum feed displacement should be $d_{max} = D/4$. On one hand, for a certain $d_i$, larger $\theta_{edge}$ (smaller $F/D$) leads to higher steering angles, $\psi_i$. On the other hand, $\theta_c$ appears at a smaller angle when the lens is illuminated off-focus [$\theta_c^{d_i}$ in Fig. 8(a)], and so the lens should be truncated at $\theta_{edge}$ smaller than $\theta_c^{d_i}$ (larger $F/D$) to avoid significant reflection loss. In this way, the optimum $\theta_{edge}$ which maximizes the steering angle should fulfill $\theta_{edge} = \theta_c^{d_{max}}$, for $d_{max} = D/4$. This criterion is independent of the lens $D$. Fig. 3(b) shows the optimum $\theta_{edge}$ for different $\varepsilon_r$, extracted with the described approach. For lenses with $\varepsilon_r$ between 2 and 12, the optimum $\theta_{edge}$ stays around 20° in all cases. Fig. 8 shows the corresponding $\psi_{max}$ calculated geometrically (triangles).

The calculated optimum $\theta_{edge}$ has been validated with a single-plane Physical Optics tool, extracting $\psi_{max}$ for which $\eta_{ap}$ decays 3 dB with respect to broadside. Lenses with $D = 18\lambda_0$ are considered, illuminated by cosine patterns with $-11$ dB taper at the lens edge. The results are shown in Fig. 8(b), being the optimum $\theta_{edge}$ near 18° for all studied cases, validating the geometric approximation [Fig. 3(b)]. The maximum steering angles extracted here for $\varepsilon_r = 12$ are 27° and 30° for the H- and E-planes, respectively, for truncated lenses with $\theta_{edge} = 18°$ and adapted ideal cosine feeds. These steering angles are higher than in the case of the silicon lenses considered in [29], where a maximum scan angle of 20° was reported for $\theta_{edge} \sim 60°$ [off-scale in Fig. 8(b)].

When using the LWA as a feeder, in case of $\varepsilon_r = 6$, the optimum lens $\theta_{edge}$ values which maximize $\eta_{il}$ at broadside and $\psi_{max}$ for steering are nearly coincident [see Fig. 3(b)]. In case of $\varepsilon_r < 6$, the optimum $\theta_{edge}$ for the lens broadside beam is larger than the optimum $\theta_{edge}$ for maximum steering. The maximum number of beams is limited, in this case, by the increment in the reflection loss due to the larger total-reflection area. In case of $\varepsilon_r > 6$, the optimum $\theta_{edge}$ for the broadside beam is smaller than the optimum $\theta_{edge}$ for steering. Here, the maximum steering angle reached is limited by the increasing spillover loss, due to the larger $F/D$ ratio.

The achieved steering angles with the LWA patterns optimized for broadside [Fig. 5 (right)] have been calculated using an *ad hoc* PO tool considering the whole lens surface [30]. The results are plotted in Fig. 8(b) for $\varepsilon_r = 2.3$, 6, and 12 (circles). The PO simulated results for the LWA have been validated via FW simulations (no multiple reflections) carried out with the software EMPIRE-XPU [31]. The results are in good agreement, as shown in Fig. 9.

Coming back to the scope of this analysis, the number of beams achieved per plane considering lenses with LW feeders and $D = 18\lambda_0$ can be evaluated from the maximum steering angle and the $-3$ dB beamwidth (∼3.5°) as follows: 7 beams ($\psi_{max} = 12.5°$) with $\varepsilon_r = 2.3$, 12 beams ($\psi_{max} = 21.5°$) with $\varepsilon_r = 6$, and 11 beams ($\psi_{max} = 19.75°$) with $\varepsilon_r = 12$. In a two-dimensional circular planar array of lenses, those steering angles correspond to 40, 110, and 90 beams for $\varepsilon_r = 2.3$, 6, and 12, respectively. In the multifixed beam scenarios introduced in Section I, each beam corresponds to one feed antenna and transceiver.

## VI. BROADBAND PROTOTYPE

From the analyses in previous sections, the optimal lens material for this application seems to be $\varepsilon_r = 2.3$, since it presents the highest efficiency and widest bandwidth. In addition, due to the lens low $\varepsilon_r$, there is no need to use a matching layer, which added to the lower material cost results in the most cost-effective approach. The only compromise made when choosing a lens with low $\varepsilon_r$ is the reduction in the potential field of view achievable with a Fly's eye array [Fig. 1(b)], as discussed in Section V. In this section, a design covering the whole $G$-band (140–220 GHz) is presented, using an HDPE lens ($\varepsilon_r = 2.3$, tan$\delta = 0.00033$). This material has been chosen after characterizing several plastics in the frequency range of interest, as it presented the lowest measured dielectric loss. As the final step, a fine tuning of the double-slot geometry is carried out in order to achieve a good impedance matching to the waveguide over the whole frequency band. The analytic primary patterns calculation and lens aperture efficiency computation are validated for the final optimized model by means of FW simulations.

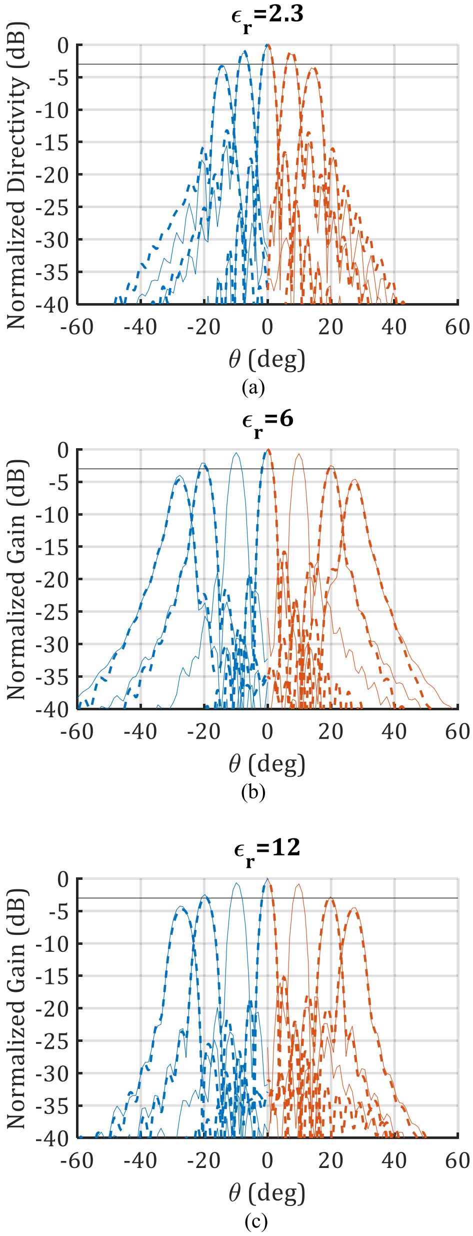

(a)

(b)

(c)

Fig. 9. Lens far-field magnitude simulated with a 2-D PO (solid line) and FW without multiple reflections (dashed line), normalized to the broadside beam. The lenses ($D = 18\lambda_0$) and LWA feeds are optimized for maximum $\eta_{il}$ at broadside (Section IV). (a) $\varepsilon_r = 2.3$ for $d = 0$, 0.08, and 0.16 D. (b) $\varepsilon_r = 6$ for $d = 0$, 0.11, 0.23, and 0.30 D. (c) $\varepsilon_r = 12$ for $d = 0$, 0.13, 0.25, and 0.34 D. Blue: E-plane. Red: H-plane. A black line marks the 3 dB scan loss criterion for maximum steering angle.

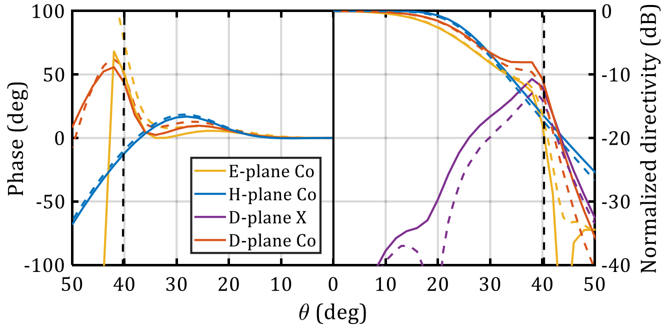

Fig. 10. Feed radiation patterns and phase for the fabricated prototype at $f_0$. Solid lines: SGF solution, dashed lines: FW simulations. The prototype lens $\theta_{edge}$ is marked with dashed black lines.

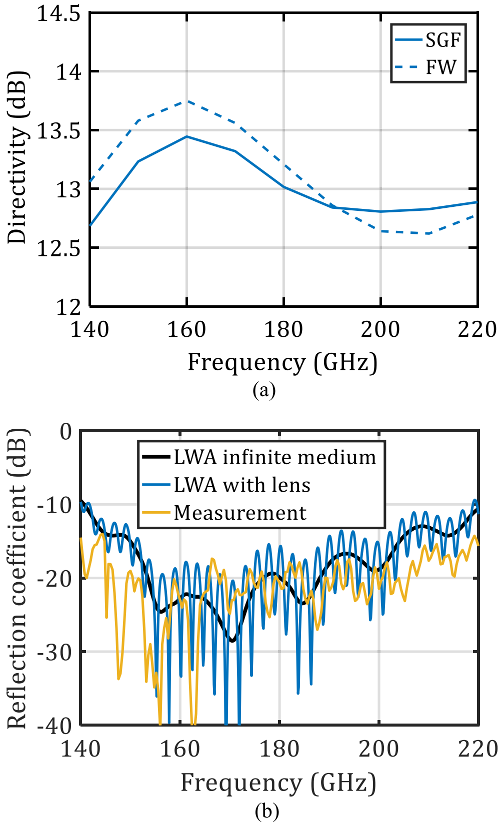

(a)

(b)

Fig. 11. (a) Maximum directivity over frequency for the prototype LWA radiating in the semi-infinite medium and (b) LWA reflection coefficient.

### A. Feed radiation patterns and impedance matching

The final geometrical values of the optimized double-slot iris are set to $\alpha = 65.5°$, $t = 0.08\lambda_0$, $\rho_0 = 0.54\lambda_0$, $w = 0.3\lambda_0$, and the cavity $h = 0.56\lambda_0$ (Fig. 2), being $\lambda_0$ to the wavelength at $f_0 = 180$ GHz. The slots have been widened to reach a good impedance matching; $\rho_0$ has been slightly increased with respect to the optimum. The impact of those small variations in the $\eta_{il}$ is negligible, as will be shown in the next subsection. Fig. 10 shows the radiation pattern magnitude and phase at $f_0$, while Fig. 11(a) shows the maximum directivity over frequency. In both cases, there is a good agreement between analytically computed results and FW simulations, validating the approximate expression of the iris current distribution introduced in (8) (Appendix). The maximum variation in the lens LWA feed directivity over the entire frequency band is around 1 dB. Fig. 11(b) shows the FW simulation results for the LWA reflection coefficient radiating in a semi-infinite medium and inside the lens (including multiple reflections), in both cases lower than $-10$ dB over the whole operational bandwidth. The FW simulation model is done with perfect electric conductor boundary conditions and includes a taper from a standard flange to a squared waveguide [Fig. 2(a) and (c)].

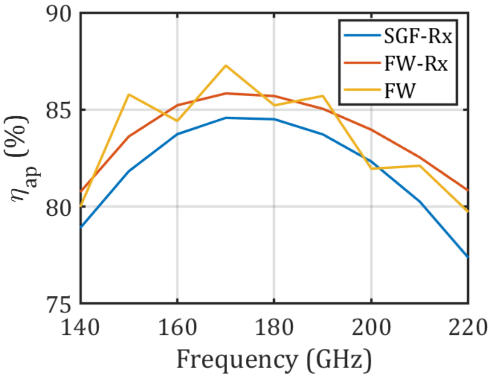

Fig. 12. Lens $\eta_{ap}$ over frequency obtained with the reception analysis using the SGF primary pattern with the double-slot current approximation (SGF-Rx) and the FW simulated primary pattern (FW-Rx), together with an FW simulation with multiple reflections, which introduce a small ripple.

### *B. Lens Radiation Performance*

In this section, the simulation results for a *G*-band HDPE lens with $D = 3$ cm are shown. After tuning the double-slot geometry in order to achieve a good matching over the whole bandwidth, a fine readjustment of the feed $\Delta z$ and lens $\theta_{edge}$ has been performed to maximize the lens $\eta_{ap}$, applying the reception analysis described in Section III. The final value for $\theta_{edge}$ is 40.3°, slightly smaller than the optimum displayed in Section IV due to the higher taper in the E-plane, caused by the larger $\rho_0$. The final $\Delta z$ has been set to –0.95 mm.

The resulting $\eta_{ap}$ is displayed in Fig. 12. Here, the analysis in reception (Rx) has been applied on one side to the primary patterns calculated with the SGF convoluted with the current approximation for the double slot (SGF-Rx) and on the other side to the FW primary patterns (FW-Rx), validating (8) over the whole frequency band. FW simulations with the lens, including multiple reflections, have been performed in order to validate the lens $\eta_{ap}$ optimization and analysis in reception (Fig. 12) and to obtain the lens far-field radiation patterns (Fig. 13). The good agreement between the $\eta_{ap}$ obtained through the analysis in reception and FW simulation proves that the multiple reflections and possible spillover do not have any significant impact on the lens antenna far-fields, due to the lens low $\varepsilon_r$. The FW simulation results show $\eta_{ap}$ higher than 80% in the whole frequency band. The achieved bandwidth is also marked in Fig. 7, reaching almost identic values with respect to the ideal case.

In Fig. 13, the normalized simulated co-polarized patterns for the broadside and two steered beams are shown. The highest lens cross-polar level at broadside normalized to the copolar maximum directivity is –20 dB at 140 GHz. The co-polar gain over frequency is displayed in Fig. 14, corresponding the lens $\eta_{ap}$ drop in the steered beams to the expected from the analysis in Section V. The maximum estimated ohmic loss in the lens dielectric material is about 0.5 dB at the highest frequency (220 GHz). The ohmic losses in the 1 cm-long waveguide are between 0.8 and 1.5 dB in the whole frequency band, for an estimated effective metal conductivity of 3.6e5 S/m. The conductor loss could be significantly reduced in an integrated design by shortening the waveguide and improving its roughness. Table II summarizes the estimated loss contributions for a single lens.

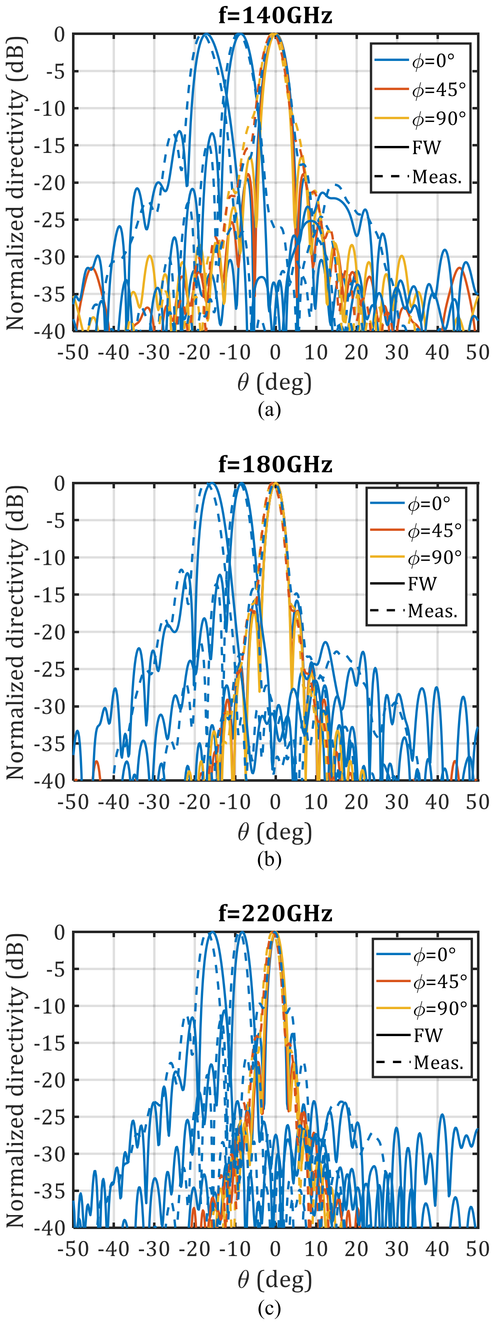

(a)

(b)

(c)

Fig. 13. FW simulated (multiple reflections) and measured lens patterns normalized to each beam maximum, at (a) 140 GHz, (b) 180 GHz, and (c) 220 GHz. The steered beams correspond to feed displacements, $d = 2.8$ and 5.6 mm, for which the measured steering angle is 9.25° and 18.25° for 140 GHz, 9° and 17.25° for 180 GHz, and 9° and 17° for 140 GHz, respectively.

## VII. FABRICATION AND MEASUREMENTS

Two identical prototypes have been fabricated consisting of three main parts: an aluminum split-block waveguide tapered to a standard waveguide flange, a thin metal plate containing

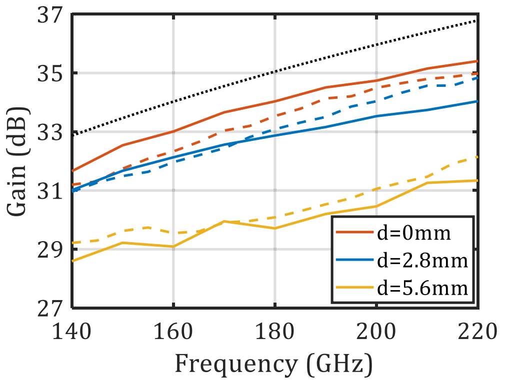

Fig. 14. Gain over frequency for broadside and steered beams. Solid line: FW simulations. Dashed line: measurements. These results do not include loss in the waveguide. Dotted black curve: maximum directivity for a circular aperture with $D = 3$ cm.

TABLE II

LOSSES IN THE FABRICATED PROTOTYPE

| Freq. | Waveguide | Mismatch | Dielectric |
|---|---|---|---|
| 140GHz | 1.48dB | 0.31dB | 0.24dB |
| 180GHz | 0.88dB | 0.02dB | 0.32dB |
| 220 GHz | 0.86dB | 0.14dB | 0.40dB |

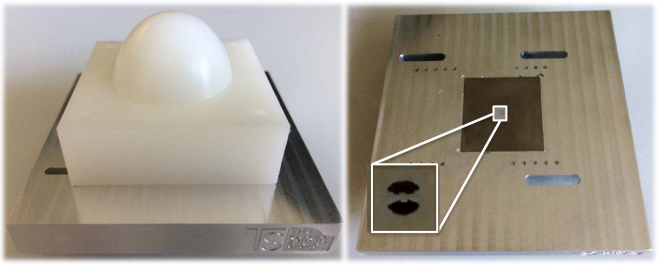

Fig. 15. Lens antenna prototype. The left-hand side shows the HDPE lens antenna, placed on the ground plane. On the right-hand side, the double-slot iris is shown. Positioning holes have been drilled at a constant distance of 1.4 mm, to displace the lens and measure the broadside and steered beams.

the double-slot iris, and the HDPE lens with the air cavity. Fig. 15 shows a picture of one of the fabricated prototypes. The waveguide and lens have been manufactured through standard milling techniques, whereas the double-slot iris has been realized by means of laser cut. The measured reflection coefficient is in accordance with the simulations [Fig. 11(b)]. The matching level shift between the lossless FW simulations and measurements is related to the waveguide ohmic losses.

Applying the analysis in reception explained in the Appendix, the near-field coupling between two identical lenses, $\eta_c$, facing each other is calculated [Fig. 16(a)]. This parameter, which can be measured with a simple setup, can be used to determine the single-antenna radiation efficiency and, therefore, gain, and to evaluate the accuracy of the estimated losses in the lens and waveguide. Fig. 16(c) shows the lens-to-lens near-field coupling calculated semianalytically, FW simulated, and measured, with the reference plane at the standard waveguide flanges. In the semi-analytic calculation, mismatch loss, losses in the waveguide, and dielectric loss in the lens (Table II) have been added to the near-field coupling calculated with the analysis in reception. The transmission between two lenses in the FW simulation does not include multiple reflections. The difference between both curves shows the limitation in the accuracy of the GO approach used for the analytic calculation of the transmitted fields after the lens, $\vec{E}_{GO}^{S_c}$. In the lens-to-lens near-field coupling measurements, time gating has been applied to eliminate the contribution of multiple reflections in the lens–air interfaces. The time gating has been performed applying a window which considers only the first transmitted rays from one lens to the other as shown in Fig. 16(b). All additional transmitted rays coming from multiple reflections inside the lenses or between them are filtered in time domain, and finally, the resulting frequency response is extracted from the filtered results [plotted in Fig. 16(c)]. The time-gated measurement results show an agreement with the FW simulations within ±1 dB in the worst case, which is translated in ±0.5 dB for a single lens. This error includes the impact of tolerances in the measurement, fabrication, and material properties estimation, such as lens $\tan\delta$ and waveguide-effective conductivity.

An FW simulation has been performed eliminating the lenses and keeping the LWA feeds in the same position (the space between feeders is filled with dielectric). The transmission reached in this configuration is lower than $-30$ dB in the whole band. This value corresponds to the directivity of both feeds ($13 \pm 0.5$ dB) minus the propagation loss in the dielectric material (55–59 dB). The presence of the lenses improves the coupling in 27–31 dB.

In order to obtain the lens far-field patterns, near-field measurements have been performed over a planar surface on top of the lens antenna, by means of a probe (i.e., an open-ended WR5 waveguide) placed on an automatic positioner. A squared surface with an area of $50 \times 50$ mm$^2$ has been measured at 8.5 cm distance from the lens, taking sampling points at 680 $\mu$m distance (half wavelength at the highest frequency, 220 GHz). Around the measuring probe, a hollow metallic diffraction cone has been installed, in order to minimize the effect of multiple reflections between the lens and measurement equipment. A standard probe correction has been then applied to remove the small impact of the probe in the measured far-field, with the same approach presented in [32]. Fig. 13 compares the measured and FW simulated lens far-field patterns for broadside and two steered beams, showing an excellent agreement over the whole frequency band. This can be also seen in the results for the maximum gain over frequency shown in Fig. 14. The maximum antenna gain at broadside has been estimated by adding the dielectric loss, validated with the lens-to-lens coupling method, to the directivity extracted from the near-field measurements. In case of the steered beams, the gain has been evaluated by normalizing the radiation intensity with the power radiated

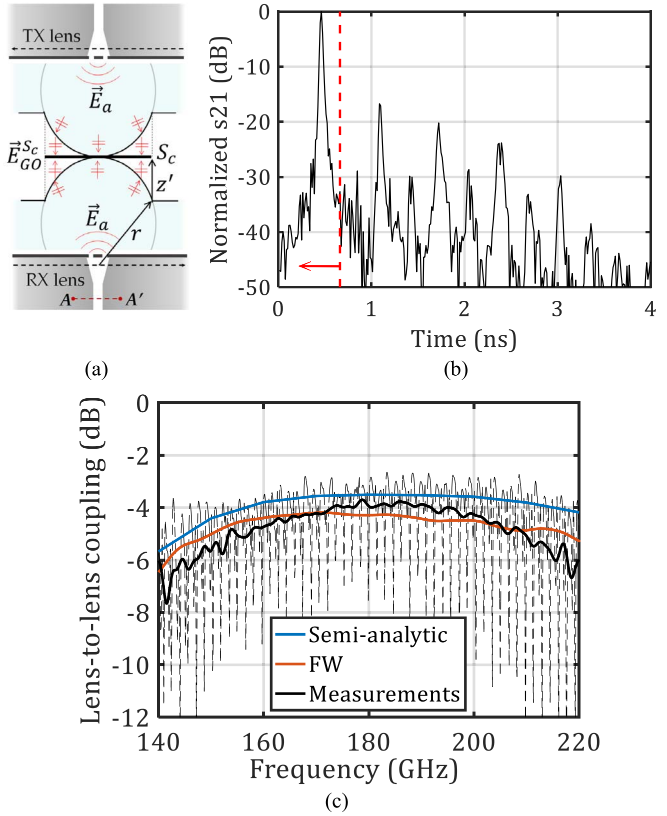

(a) (b)

(c)

Fig. 16. (a) Analysis in reception of lens-to-lens near-field coupling. (b) Time-domain representation of the measured transmission between the two lenses. The red dashed line marks the applied time window. (c) Lens-to-lens near-field coupling efficiency where the black lines correspond to the measured S21: raw (dashed) and time gated (solid).

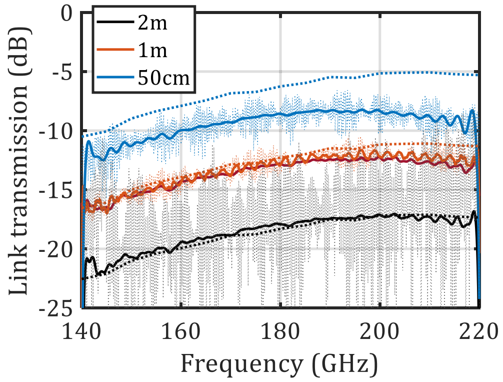

Fig. 17. Measured and estimated transmissions between two lenses placed at large distances. Thin dashed lines: raw transmission measurements. Solid lines: measurements after time gating. Dotted lines: results estimated with Friis equation. Results include both dielectric loss and conductor loss. For 1 m distance, light red: measurement in transmission; dark red: measurement in reflection.

and dielectric loss of the broadside case. The losses in the waveguide are not included in this plot. These results confirm that 7 beams in a linear array or 40 beams in a two-dimensional array configuration can be achieved with an HDPE lens planar array, with a maximum scan loss of 3 dB. The maximum difference between the FW simulated and measured maximum directivities is 0.7 dB in the whole bandwidth and for all the measured beams, which is related to the measurement and fabrication tolerances. Several measurements were performed changing the measurement plane height. Measurement repeatability showed changes in the estimated directivity of around 0.5 dB.

The transmission between two lenses placed at different distances (50 cm, 1 m and 2 m) has been as well measured in order to validate the antenna gain estimation. Fig. 17 shows the raw and time-gated measurement results compared to the transmission calculated with Friis equation. The measured results converge to the estimation with Friis equation when the link distance approaches 2 m, where both lenses can be considered to be at far-field distance. The link measurement with 2 m distance presents higher ripple, since it was performed with a single lens placed in front of a metal plate at 1 m distance, due to the lack of cables reaching this length. This measurement in reflection has been as well performed placing the metal plate at 50 cm distance, showing the same results as the measured transmission between two lenses at 1 m distance (Fig. 17).

## VIII. CONCLUSION

An analytical design methodology based on an analysis in reception is proposed to optimize the truncated elliptical lenses fed with resonant LWAs. With this aim, the aperture efficiency is expressed as a reaction integral between the lens inward spherical GO field and the field radiated by the LW feed inside the lens. Both fields can be analytically evaluated, simplifying the optimization of the lens antenna with respect to other full-wave or PO techniques. Applying this analysis in reception, design rules are derived for the use of the LWA as a feeder for elliptical lenses with different $\varepsilon_r$. Optimum geometric parameters for the feeder and lens are extracted, showing the maximum illumination efficiency and bandwidth reached for each lens $\varepsilon_r$. The steering capabilities for truncated elliptical lenses are also displayed for different $\varepsilon_r$. Following the proposed design rules, the best compromise between illumination efficiency and steering capabilities can be selected depending on the application.

A broadband integrated lens antenna is presented for future wireless communications at high frequencies. The proposed antenna is based on the resonant leaky-wave feed coupled to an HDPE elliptical lens. This design represents a trade-off with high efficiency, very large bandwidth, and low cost but limited number of off-focus beams. The lens achieves 34 dB gain at 180 GHz, reaching an aperture efficiency higher than 80% and ohmic losses lower than 0.5 dB over 44% relative bandwidth for the broadside beam. This design enables to generate up to 40 beams overlapping at $-3$ dB with a planar two-dimensional Fly's eye array of lenses, keeping the gain higher than 30 dB at 180 GHz. The reflection coefficient is lower than $-10$ dB over the whole frequency band. The antenna has been fabricated and measured, showing excellent agreement with the simulated performances.

## APPENDIX

### A. Lens Analysis in Reception

In [33], an analysis in reception for the optimization of reflector feeds was proposed. The power received by the feed can then be estimated using a Thevenin equivalent circuit when the reflector is illuminated with a plane wave. The open circuit voltage at the defined terminals can be expressed as a reaction field integral between the considered problem in reception and an equivalent problem in transmission. The generalization of this procedure to any geometry via the use of the equivalence theorem was described in [34]. In this appendix, a similar methodology is applied to analyze the proposed lens antenna geometry [see Fig. 3(a)].

### B. Thevenin Equivalent Circuit

An equivalent Thevenin circuit for the problem in Fig. 3(a) can be derived by evaluating the open circuit induced by the incident plane wave onto the antenna terminals, *AA'*, inside the waveguide, the antenna input impedance $Z_a$, and the load impedance $Z_L$ [Fig. 18(b)]. The open circuit field inside a single mode waveguide can be expressed as $\vec{E}_{oc} = V_{oc}\vec{e}_0$, where $\vec{e}_0$ is the electric-field-associated eigenvector of the considered waveguide mode (TE$_{01}$ in this case). The open circuit voltage, $V_{oc}$, can be evaluated as

$$V_{oc} = \iint_{S_{AA'}} \vec{E}_{oc} \cdot \vec{e}_0 dS. \tag{3}$$

The power dissipated in a matched load ($Z_a^* = Z_L$) can be calculated as $P_L = |V_{oc}|^2/(8R_a)$, being $R_a = Re(Z_a)$ the antenna radiation resistance.

### C. Reaction Integral

The value of the open-circuit voltage, $V_{oc}$ in (3), necessary to evaluate the received power, $P_L$, can be expressed as a reaction integral between the open-circuit field in the antenna in reception and the equivalent currents characterizing the same antenna in transmission. Let us consider the antenna in transmission fed by an electric current, $\vec{J}_{tx}$, with arbitrary amplitude, $I_{tx}$. This current is related to the magnetic field by $\vec{J}_{tx} = -\hat{z} \times \vec{H} = -\hat{z} \times I_{tx}\vec{h}_0$, where $\vec{h}_0$ is the magnetic-field-associated eigenvector of the considered waveguide mode. Since $\vec{e}_0 = \hat{z} \times \vec{h}_0$, the integral in (3) can be then expressed as

$$V_{oc}I_{tx} = -\iint_{S_{AA'}} \vec{E}_{oc} \cdot \vec{J}_{tx} dS. \tag{4}$$

The antenna radiation resistance, $R_a$, can at the same time be related to the power radiated by the antenna, $P_{rad}$, excited by the same current amplitude, $I_{tx}$, as $P_{rad} = (|I_{tx}|^2/2)R_a$. Thus, $P_L$ can be expressed using the reaction integral in (4) as

$$P_L = \frac{|V_{oc}I_{tx}|^2}{16P_{rad}}. \tag{5}$$

Equation (5) was reported in [34]. Note that the actual amplitude of the equivalent current in transmission, $I_{tx}$, cancels out in this expression. Once we have expressed the received power as a reaction integral between two different problems (currents in transmission and open circuit field in reception), we can use the reciprocity theorem to change this reaction integral to any surface, by interchanging fields and currents between both problems.

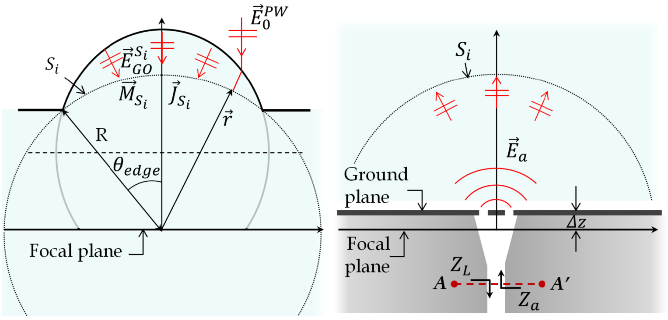

(a) (b)

Fig. 18. (a) Boundary conditions to calculate the incident field, $\vec{E}_{GO}^{S_i}$, from the ideal plane wave impinging the lens, $\vec{E}_0^{PW}$, and associated induction currents in $S_i$, $\vec{M}_{S_i}$, and $\vec{J}_{S_i}$. (b) Boundary conditions to calculate the fields radiated in transmission mode, $\vec{E}_a$.

### D. Aperture Efficiency Calculation

In order to carry out the lens optimization, the most convenient surface to perform the reaction integral is the spherical surface $S_i$, shown in Fig. 3(a) and Fig. 18, defined as close as possible to the lens surface, since here all fields involved in the reaction integral can be analytically evaluated. In the equivalent problem in reception, the field induced by the incident plane wave at the open-circuited antenna terminals, $\vec{E}_{oc}$, can be evaluated by means of a set of surface equivalent currents $\vec{M}_{S_i}$ and $\vec{J}_{S_i}$ at $S_i$. In the equivalent problem in transmission, the fields radiated by the feed antenna excited by $\vec{J}_{tx}$, $[\vec{E}_a, \vec{H}_a]$, should be evaluated at $S_i$ in the presence of the lens. We can, therefore, apply the reciprocity theorem and reformulate (4) as

$$V_{oc}I_{tx} = \iint_{S_i} (\vec{H}_a \cdot \vec{M}_{S_i} - \vec{E}_a \cdot \vec{J}_{S_i}) dS. \tag{6}$$

This expression can be further simplified. On one side, the equivalent currents $\vec{M}_{S_i}$ and $\vec{J}_{S_i}$ used in (6) can be approximated using a GO field propagation $[\vec{E}_{GO}^{S_i}, \vec{H}_{GO}^{S_i}]$ evaluated in the absence of the antenna feed [Fig. 18(a)], as $\vec{M}_{S_i} = \vec{E}_{GO}^{S_i} \times \hat{n}$ and $\vec{J}_{S_i} = \hat{n} \times \vec{H}_{GO}^{S_i}$ being $\hat{n} = -\hat{r}$. The analytical expression of these fields in an elliptical lens was given in [26]. The diffracted fields are neglected, since $S_i$ is taken very close to the lens surface. On the other side, neglecting the impact of the multiple reflections at the lens–air interface, the radiated fields $[\vec{E}_a, \vec{H}_a]$ used in (6) can be approximated as the ones radiated into an infinite dielectric medium [Fig. 18(b)]. If the reaction surface $S_i$ is chosen to be in the far-field of the feed antenna, a small displacement in the z-direction of the feeding antenna with respect to the lens focal plane, $\Delta z$, [Fig. 18(b)] can be accounted with a variable phase term intrinsic in $\vec{E}_a$, as follows:

$$\vec{E}_a(\theta,\phi) = \vec{E}_a^{GP}(\theta,\phi)e^{jk\Delta z cos\theta} \tag{7}$$

where $\vec{E}_a^{GP}(\theta,\phi)$ is the far-field of the antenna calculated with phase reference placed at ground plane. This field can be evaluated resorting to an asymptotic evaluation of the spectral Green's function for stratified media [23], with the following approximation of the double-slot iris current:

$$\begin{aligned}&\vec{m}_s(\rho,\phi)\\&\approx \frac{1}{\rho}\cos\left(\frac{\pi}{2\alpha}\left(\phi\pm\frac{\pi}{2}\right)\right) rect(\phi\pm\frac{\pi}{2},2\alpha)rect(\rho-\rho_0/2,w)\hat{x}\end{aligned} \tag{8}$$

where $\alpha$, $\rho_0,$ and $w$ are the parameters describing the iris geometry [Fig. 2(b)]. Since both the GO incident field, $\vec{E}_{GO}^{S_i}$, and the far-field radiated by the antenna, $\vec{E}_a$, are spherical waves, (6) can be simplified into

$$V_{oc}I_{tx} = \frac{2}{\zeta_d}\int_0^{2\pi}\int_0^{\theta_{edge}} \vec{E}_{GO}^{S_i}(\theta,\phi)\cdot\vec{E}_a^{GP}(\theta,\phi)e^{jk\Delta zcos\theta}dS \tag{9}$$

where $\zeta_d$ is the wave impedance in the lens medium.

### E. Lens-to-Lens Near-Field Coupling Efficiency

In order to determine the near-field coupling efficiency $\eta_c$ between two lenses [Fig. 16(a)], one of them is considered in transmission mode, whereas the other is analyzed in reception. In this way, the field impinging the receiving lens corresponds to the field radiated by the lens considered in transmission. $\eta_c$ is then calculated as the ratio between the power dissipated at the receiving lens load, $P_L$, and the power radiated by the transmitting lens feed, $P_{rad}$. Following similar steps than in the previous sections, the term $V_{oc}I_{tx}$ can be determined as the reaction integral between the fields transmitted by both lenses, $[\vec{E}_{GO}^{S_c}, \vec{H}_{GO}^{S_c}]$, in the plane between the two lenses [$S_c$ in Fig. 16(a)]. This analysis neglects the impact of multiple reflections, inside and between both lenses. The fields transmitted at $S_c$ can be approximated using a GO approach, where the rays are assumed to be propagating in the z-direction with a uniform phase front (valid only when the feed's phase center is at the ellipse's focus). For such case

$$\vec{E}_{GO}^{S_c}(\rho,\phi) = [\tau_\parallel(\rho)(\vec{E}_a(\vec{r})\cdot\hat{\theta})\hat{\rho}+\tau_\perp(\rho)(\vec{E}_a(\vec{r})\cdot\hat{\phi})\hat{\phi}]e^{-jk_0z'} \tag{10}$$

being $\vec{r}$ the vector defining the lens surface, $z'$ the distance between the lens surface and the integration plane [Fig. 16(a)], and $\tau_\parallel$ and $\tau_\perp$ the parallel and perpendicular Fresnel transmission coefficients as defined in [8], respectively. Since the propagation of the transmitted field from the lens surface up to $S_c$ assumes all transmitted rays to be propagating perpendicularly to $S_c$, the near-field coupling efficiency, $\eta_c$, can be expressed only as a function of the electric fields as

$$\eta_c = \frac{P_L}{P_{rad}} = \frac{\left|\frac{2}{\zeta_0}\int_0^{2\pi}\int_0^{D/2}\vec{E}_{GO}^{S_c}(\rho,\phi)\cdot\vec{E}_{GO}^{S_c}(\rho,\phi)\rho d\rho d\phi\right|^2}{16P_{rad}^2}. \tag{11}$$

## REFERENCES

[1] J. Edstam, J. Hansryd, S. Carpenter, T. Emanuelsson, Y. Li, and H. Zirath, "Microwave backhaul evolution: Reaching beyond 100 GHz," Ericsson AB, Stockholm, Sweden, Tech. Rep. Ericsson Technol. Rev. Issue 2/2017, Feb. 2017.

[2] N. Llombart, D. Emer, M. Arias Campo, and E. McCune, "Fly's eye spherical antenna system for future Tbps wireless communications," in *Proc. Eur. Conf. Antennas Propag. (EuCAP)*, Paris, France, Apr. 2017.

[3] A. Hosseini, F. De Flaviis, and F. Capolino, "Design formulas for planar Fabry-Pérot cavity antennas formed by thick partially reflective surfaces," *IEEE Trans. Antennas Propag.*, vol. 64, no. 12, pp. 5487–5491, Dec. 2016.

[4] G. Minatti, M. Faenzi, M. Sabbadini, and S. Maci, "Bandwidth of gain in metasurface antennas," *IEEE Trans. Antennas Propag.*, vol. 65, no. 6, pp. 2836–2842, Jun. 2017.

[5] K. Pham *et al.*, "Design of wideband dual linearly polarized transmitarray antennas," *IEEE Trans. Antennas Propag.*, vol. 64, no. 5, pp. 2022–2026, May 2016.

[6] A. Sarkar, A. Sharma, A. Biswas, and M. J. Akhtar, "EMSIW-based compact high gain wide full space scanning LWA with improved broadside radiation profile," *IEEE Trans. Antennas Propag.*, vol. 67, no. 8, pp. 5652–5657, Aug. 2019.

[7] Y. Geng, J. Wang, Y. Li, Z. Li, M. Chen, and Z. Zhang, "New design of beam-formed leaky-wave antenna based on substrate integrated waveguide in a confined space," *IEEE Trans. Antennas Propag.*, vol. 66, no. 11, pp. 6334–6339, Nov. 2018.

[8] D. Filipovic, S. Gearhart, and G. Rebeiz, "Double-slot antennas on extended hemispherical and elliptical silicon dielectric lenses," *IEEE Trans. Microw. Theory Techn.*, vol. 41, no. 10, pp. 1738–1749, Oct. 1993.

[9] N. T. Nguyen, N. Delhote, M. Ettorre, D. Baillargeat, L. Le Coq, and R. Sauleau, "Design and characterization of 60-GHz integrated lens antennas fabricated through ceramic stereolithography," *IEEE Trans. Antennas Propag.*, vol. 58, no. 8, pp. 2757–2762, Aug. 2010.

[10] A. J. Alazemi, H.-H. Yang, and G. M. Rebeiz, "Double bow-tie slot antennas for wideband millimeter-wave and terahertz applications," *IEEE Trans. THz Sci. Technol.*, vol. 6, no. 5, pp. 682–689, Sep. 2016.

[11] A. Neto, "UWB, non dispersive radiation from the planarly fed leaky lens antenna—Part 1: Theory and design," *IEEE Trans. Antennas Propag.*, vol. 58, no. 7, pp. 2238–2247, Jul. 2010.

[12] N. Llombart, G. Chattopadhyay, A. Skalare, and I. Mehdi, "Novel terahertz antenna based on a silicon lens fed by a leaky wave enhanced waveguide," *IEEE Trans. Antennas Propag.*, vol. 59, no. 6, pp. 2160–2168, Jun. 2011.

[13] N. Llombart *et al.*, "Silicon micromachined lens antenna for THz integrated heterodyne arrays," *IEEE Trans. THz Sci. Technol.*, vol. 3, no. 5, pp. 515–523, Sep. 2013.

[14] A. Artemenko, A. Mozharovskiy, A. Maltsev, R. Maslennikov, A. Sevastyanov, and V. Ssorin, "Experimental characterization of E-band two-dimensional electronically beam-steerable integrated lens antennas," *IEEE Antennas Wireless Propag. Lett.*, vol. 12, pp. 1188–1191, 2013.

[15] J. R. Costa and C. A. Fernandes, "Broadband slot feed for integrated lens antennas," *IEEE Antennas Wireless Propag. Lett.*, vol. 6, pp. 396–400, 2007.

[16] J. Costa, M. Silveirinha, and C. Fernandes, "Evaluation of a double-shell integrated scanning lens antenna," *IEEE Antennas Wireless Propag. Lett.*, vol. 7, pp. 781–784, 2008.

[17] X. Wu, G. Eleftheriades, and T. van Deventer-Perkins, "Design and characterization of single- and multiple-beam mm-wave circularly polarized substrate lens antennas for wireless communications," *IEEE Trans. Microw. Theory Techn.*, vol. 49, no. 3, pp. 431–441, Mar. 2001.

[18] J. Ala-Laurinaho *et al.*, "2-D beam-steerable integrated lens antenna system for 5G E-band access and backhaul," *IEEE Trans. Antennas Propag.*, vol. 64, no. 7, pp. 2244–2255, Jul. 2016.

[19] K. Konstantinidis *et al.*, "Low-THz dielectric lens antenna with integrated waveguide feed," *IEEE Trans. THz Sci. Technol.*, vol. 7, no. 5, pp. 572–581, Sep. 2017.

[20] N. Llombart, A. Neto, G. Gerini, M. Bonnedal, and P. De Maagt, "Impact of mutual coupling in leaky wave enhanced imaging arrays," *IEEE Trans. Antennas Propag.*, vol. 56, no. 4, pp. 1201–1206, Apr. 2008.

[21] N. Llombart, A. Neto, G. Gerini, M. Bonnedal, and P. De Maagt, “Leaky wave enhanced feed arrays for the improvement of the edge of coverage gain in multibeam reflector antennas,” *IEEE Trans. Antennas Propag.*, vol. 56, no. 5, pp. 1280–1291, May 2008.

[22] D. Jackson, A. Oliner, and A. Ip, “Leaky-wave propagation and radiation for a narrow-beam multiple-layer dielectric structure,” *IEEE Trans. Antennas Propag.*, vol. 41, no. 3, pp. 344–348, Mar. 1993.

[23] A. Neto, N. Llombart, G. Gerini, M. D. Bonnedal, and P. De Maagt, “EBG enhanced feeds for the improvement of the aperture efficiency of reflector antennas,” *IEEE Trans. Antennas Propag.*, vol. 55, no. 8, pp. 2185–2193, Aug. 2007.

[24] A. Neto and N. Llombart, “Wideband localization of the dominant leaky wave poles in dielectric covered antennas,” *IEEE Antennas Wireless Propag. Lett.*, vol. 5, pp. 549–551, 2006.

[25] P. Burghignoli, “A leaky-wave analysis of the phase center in fabry-pérot cavity antennas,” *IEEE Trans. Antennas Propag.*, vol. 60, no. 5, pp. 2226–2233, May 2012.

[26] N. Llombart, B. Blazquez, A. Freni, and A. Neto, “Fourier optics for the analysis of distributed absorbers under THz focusing systems,” *IEEE Trans. THz Sci. Technol.*, vol. 5, no. 4, pp. 573–583, Jul. 2015.

[27] C. A. Balanis, *Antenna Theory: Analysis and Design*, 3rd ed. Hoboken, NJ, USA: Wiley, 2005.

[28] D. Blanco, E. Rajo-Iglesias, S. Maci, and N. Llombart, “Directivity enhancement and spurious radiation suppression in leaky-wave antennas using inductive grid metasurfaces,” *IEEE Trans. Antennas Propag.*, vol. 63, no. 3, pp. 891–900, Mar. 2015.

[29] D. Filipovic, G. Gauthier, S. Raman, and G. Rebeiz, “Off-axis properties of silicon and quartz dielectric lens antennas,” *IEEE Trans. Antennas Propag.*, vol. 45, no. 5, pp. 760–766, May 1997.

[30] O. Yurduseven, D. Cavallo, G. Carluccio, A. Neto, and M. Albani, “Parametric analysis of extended hemispherical dielectric lenses fed by a broadband connected array of leaky-wave slots,” *IET Microw., Antennas Propag.*, vol. 9, no. 7, pp. 611–617, May 2015.

[31] *EMPIRE XPU*. Accessed: 2019. [Online]. Available: http://www.empire.de

[32] E. Joy, W. Leach, and G. Rodrigue, “Applications of probe-compensated near-field measurements,” *IEEE Trans. Antennas Propag.*, vol. AP-26, no. 3, pp. 379–389, May 1978.

[33] V. Rumsey, “On the design and performance of feeds for correcting spherical aberration,” *IEEE Trans. Antennas Propag.*, vol. AP-18, no. 3, pp. 343–351, May 1970.

[34] A. Freni, N. Llombart, O. Yurduseven, and A. Neto, “On the use of thevenin circuits in distributed transmission lines and its consequences for antennas in reception,” in *Proc. Eur. Conf. Antennas Propag. (EuCAP)*, Davos, Switzerland, Apr. 2016.

**Marta Arias Campo** (Student Member, IEEE) received the M.Sc. degree in telecommunications engineering from the Universidad Politécnica de Madrid, Madrid, Spain, in 2009. She is currently pursuing the Ph.D. degree in the Terahertz Sensing Group, Technical University of Delft, Delft, The Netherlands, in collaboration with IMST GmbH, Kamp-Lintfort, Germany.

In 2009, she joined the Antennas and EM Modeling Department, IMST GmbH, where she currently works as a Research and Development Antenna Engineer in the Antenna Front-ends Team, with the main focus on the design of active planar antenna arrays. In 2016, she joined the Terahertz Sensing Group, Technical University of Delft, Delft, The Netherlands. Her research interests include the analysis and design of lens antennas and quasi-optical structures for high-speed wireless communications and radar applications.

**Darwin Blanco** received the B.Sc. degree in electrical engineering from the University of Antioquia, Medellín, Colombia, in 2009 and the M.Sc. and Ph.D. (*summa cum laude*) degrees in multimedia and communications from the University Carlos III de Madrid, Madrid, Spain, in 2011 and 2014, respectively.

He joined as a Post-Doctoral Researcher with the Université de Rennes 1, Rennes, France, from 2015 to 2016. In 2017, he worked as a Post-Doctoral Researcher with the THz Sensing Group, Technical University of Delft, Delft, The Netherlands. In 2019, he joined Ericsson AB, Göteborg, Sweden, where he is currently working as a Research and Development Antenna Engineer. His research interests include leaky-wave antennas, lens antennas, polarizers, filters, and the analysis and design of planar antennas, and periodic structures to be used in applications for phase array antennas.

**Simona Bruni** received the Laurea degree in telecommunication engineering and the Ph.D. degree in electromagnetics from the University of Siena, Siena, Italy, in 2002 and 2006, respectively. Her Ph.D. degree was financed and hosted by the Defense, Security and Safety Institute of the Netherlands Organization for Applied Scientific Research (TNO), The Hague, The Netherlands.

She worked as a Researcher with the Defense, Security and Safety Institute of the Netherlands Organization for Applied Scientific Research (TNO). From 2007 to 2013, she worked as an Research and Development Antenna Engineer with the Calearo Advanced Technology (CAT) Department, Calearo SPA, Vicenza, Italy. Since 2013, she has been with the Antennas and EM Modeling Group, IMST GmbH, Kamp-Lintfort, Germany, where she works as a Research and Development Antenna Engineer with the Antenna Front-Ends Team. Her research interests include the design of integrated antennas, high-frequency antenna arrays, and front-end design for communications and automotive applications.

**Andrea Neto** (Fellow, IEEE) received the Laurea degree (*summa cum laude*) in electronic engineering from the University of Florence, Florence, Italy, in 1994 and the Ph.D. degree in electromagnetics from the University of Siena, Siena, Italy, in 2000. Part of his Ph.D. degree was developed with the European Space Agency Research and Technology Center, Noordwijk, The Netherlands.

He worked for the Antenna Section with the European Space Agency Research and Technology Center. From 2000 to 2001, he was a Post-Doctoral Researcher with the California Institute of Technology, Pasadena, CA, USA, where he worked with the sub-mm-wave Advanced Technology Group. From 2002 to January 2010, he was a Senior Antenna Scientist with TNO Defense, Security, and Safety, The Hague, The Netherlands. In February 2010, he became a Full Professor of applied electromagnetism with the EEMCS Department, Technical University of Delft, Delft, The Netherlands, where he formed and leads the THz Sensing Group. His research interests include the analysis and design of antennas with an emphasis on arrays, dielectric lens antennas, wideband antennas, EBG structures, and terahertz antennas.

Dr. Neto is a member of the Steering Committee of the Network of Excellence NEWFOCUS, dedicated to focusing techniques in mm and sub-mm-wave regimes. In 2011, he was a recipient of the European Research Council Starting Grant to perform research on Advanced Antenna Architectures for THz Sensing Systems. He was also a recipient of the H. A. Wheeler Award for the Best Applications Paper of 2008 in the IEEE TRANSACTIONS ON ANTENNAS AND PROPAGATION, the Best Innovative Paper Prize of the 30th ESA Antenna Workshop in 2008, and the Best Antenna Theory Paper Prize of the European Conference on Antennas and Propagation (EuCAP) in 2010. In 2011, he was a recipient of the European Research Council Starting Grant to perform research on advanced antenna architectures for THz sensing systems. He served as an Associate Editor for the IEEE TRANSACTIONS ON ANTENNAS AND PROPAGATION from 2008 to 2013 and the IEEE ANTENNAS AND WIRELESS PROPAGATION LETTERS from 2005 to 2013. He is a member of the Technical Board of the European School of Antennas and Organizer of the course on antenna imaging techniques.

**Nuria Llombart** (Fellow, IEEE) received the master's degree in electrical engineering and the Ph.D. degree from the Polytechnic University of Valencia, Valencia, Spain, in 2002 and 2006, respectively. During her master's degree, she spent 1 year with the Friedrich-Alexander University of Erlangen-Nuremberg, Erlangen, Germany.

She worked with the Fraunhofer Institute for Integrated Circuits, Erlangen. From 2002 to 2007, she was with the Antenna Group, TNO Defense, Security and Safety Institute, The Hague, The Netherlands, where she was working as a Ph.D. Student and then as a Researcher. From 2007 to 2010, she was a Post-Doctoral Fellow with the California Institute of Technology, working with the Submillimeter Wave Advance Technology Group, Jet Propulsion Laboratory, Pasadena, CA, USA. She was a Ramón y Cajal Fellow with the Optics Department, Complutense University of Madrid, Madrid, Spain, from 2010 to 2012. In September 2012, she joined the THz Sensing Group, Technical University of Delft, Delft, The Netherlands, where she became a Full Professor in February 2018. She has coauthored more than 150 journals and international conference contributions. Her research interests include the analysis and design of planar antennas, periodic structures, reflector antennas, lens antennas, and waveguide structures, with emphasis in the terahertz range.

Dr. Llombart was a recipient of the H. A. Wheeler Award for the Best Applications Paper of 2008 in the IEEE TRANSACTIONS ON ANTENNAS AND PROPAGATION, the 2014 THZ SCIENCE AND TECHNOLOGY Best Paper Award of the IEEE Microwave Theory and Techniques Society, and several NASA awards. She was also a recipient of the 2014 IEEE Antenna and Propagation Society Lot Shafai Mid-Career Distinguished Achievement Award. She serves as a Board Member for the IRMMW-THz International Society. In 2015, she was a recipient of European Research Council Starting Grant.